

Continuous Adjoint Sensitivities for Optimization with General Cost Functionals on Unstructured Meshes

Oktay Baysal* and Kaveh Ghayour†
Old Dominion University, Norfolk, Virginia 23529-0236

A continuous adjoint approach is developed to obtain the sensitivity derivatives for the Euler equations. The complete derivation of the costate equations and their transversality (boundary) conditions are presented. Both the state and the costate equations are second-order finite volume discretized for unstructured meshes, and they are coupled with a constrained optimization algorithm. Also integrated into the overall methodology are a geometry parameterization method for the shape optimization, and a dynamic unstructured mesh method for the shape evolution and the consequent volume mesh adaptations. For the proof of concept, three transonic airfoil optimization problems are presented. This method accepts general cost functionals, which are not necessarily functions of pressure only. It is also shown that a switch to the natural coordinate system in conjunction with the reduction of the governing state equation to the control surface results in sensitivity integrals that are only a function of the tangential derivatives of the state variables. This approach eliminates the need for normal derivative computations that can be erroneous.

Introduction

NEARLY a decade ago, a symposium on multidisciplinary applications of computational fluid dynamics¹ included a few papers on the utilization of computational fluid dynamics (CFD) in a design environment. Since then, there has been an increase in the interest on this topic for a clearly justified reason: CFD can be useful beyond just simulating and analyzing a fluid flow and can be utilized for design optimization, to reduce the cycle time for a new product. This, however, may be prohibitive for the needed computational and human resources if, as often is the case, a large matrix of candidate designs or design variables are involved. Therefore, motivated by the need for approaches beyond cut and try, forums on CFD for design and optimization² and design optimization using CFD³ were organized. A cursory glance at Refs. 2 and 3 and other emerging publications on CFD for design should attest to the successes accomplished on the topics that include gradient-based numerical optimization methods, stochastic and genetic algorithms, shape optimization, direct and inverse methods, tradeoff identification studies, mutipoint designs, artificial-intelligence-based methods, pre- and postoptimizationsensitivity analyses, adjoint methods, and discrete and continuous sensitivity methods. The present paper will report on this last topic.

Direct numerical optimization methods are systematic methodologies, which extremize a chosen objective. They either create or merely improve a design, depending on if the global or just a local minimum has been found. However, they can be rather computing intensive, even when discrete analytical sensitivities are used. It is this very issue that motivated the present investigation. The remedy was previously explored at the numerical algorithm level^{4,5}; however, the remedy was sought at the level of the differential equations that eventually produce the directions for the search methods of the optimization process. To be more specific, first, the typical components of a simulation-based and automated design method with constraints will be itemized. These are 1) problem formulation, that is, the objective and the constraint functions; 2) gradient-based and constrained optimization algorithm; 3) flowfield simulation and analysis, that is,

CFD; 4) gradients of the objective and the constraints with respect to the design variables, that is, the sensitivity coefficients; 5) parameterization of shapes as they evolve; 6) regeneration of surface and volume grids; 7) grid sensitivities; and 8) gradients of the optimized shape with respect to the design variables, that is, the sensitivity derivatives used for tradeoff studies and off-design conditions.

The present paper will address an alternative method for the items 4) and 8), that is, to generate the pre- and postoptimization gradients. It is different from the previously published methods, which are invaluable for their respective objectives. For example, unlike Refs. 6 and 7, the present method uses unstructured meshes; unlike Refs. 8 and 9, it takes the continuous approach; and unlike Ref. 10, it accepts general cost functionals and formulates the problem in a way to produce accurate derivatives on the design surface.

Sensitivity Analysis Methods

The accuracy of a gradient-based optimization method, and the efficiency with which it can accomplish this accuracy, are directly related to the accurate and efficient receipt of the gradient information on the objectives and the constraints. The sensitivity analysis provides 1) the gradients for optimization and tradeoff studies, 2) the postoptimization gradients for off-design conditions, and 3) a first-order but inexpensive approximation to neighboring-point analysis via Taylor series expansion.¹¹ The gradient evaluation may be performed by the following approaches.¹²

Finite Difference Method

As shown in Ref. 11, this is a brute-force approach, which is highly prone to inaccuracies and inefficiencies. The computational cost of each optimization cycle scales with number of design variables plus 1 flowfield analyses. Because it is the easiest to formulate, it has been used herein to compare and validate the sensitivities obtained by the present continuous adjoint method.

Analytical Gradient Evaluation Methods

The governing equations of fluid flow can be differentiated analytically either starting with their original differential form then using the variational concepts (continuous sensitivities) or after they have been discretized (discrete sensitivities). 1) Discrete sensitivity analysis (also known as quasi analytical) is performed by differentiating already CFD-discretized equations with respect to the design variables. It corresponds to a discrete solution of the continuous sensitivity function, and they are exact. Both hand differentiation¹¹ and automatic differentiation¹³ can be used to generate the sensitivity equations. 2) In a continuous adjoint formulation (also known as

Presented as Paper 98-4904 at the AIAA/USAF/NASA/ISSMO 7th Symposium on Multidisciplinary Analysis and Optimization, St. Louis, MO, 2-4 September 1998; received 10 April 1999; revision received 16 May 2000; accepted for publication 9 June 2000. Copyright © 2000 by the American Institute of Aeronautics and Astronautics, Inc. All rights reserved.

*Professor, Eminent Scholar and Associate Dean, College of Engineering and Technology; obaysal@odu.edu. Associate Fellow AIAA.

†Graduate Research Assistant, Aerospace Engineering Department; kgghayour@caam.rice.edu.

control theory), the adjoint (or costate) equations and their boundary conditions are derived by the use of variational methods. Because these equations are of the same order and character as the flow equations, they can be discretized and solved for their Lagrange variables λ by the same CFD scheme used for the flow (or state) equations. Hence, its computer storage requirement is no more than what the flow analysis requires. Nonetheless, its analytical development may be case dependent and sometimes cumbersome. A proof-of-concept case for this formulation, for example, is given in Ref. 14 as applied to the quasi-one-dimensional Euler equations and in Ref. 15 for the two-dimensional Euler equations. The present formulation significantly improves, extends, and generalizes these methods.

Continuous Adjoint Sensitivities

Variational design optimization blends the principles of optimal control theory and the variational methods. The optimal control theory states the conditions under which the control variables, parameters, and functions, or their combinations, can be continuously altered so that the system is dictated to meet the desired criteria. The state equations considered in the present method are the Euler equations of fluid flow in conservation form:

$$\frac{\partial \mathbf{Q}}{\partial t} + \frac{\partial \mathbf{F}}{\partial x} + \frac{\partial \mathbf{G}}{\partial y} = 0 \quad (1)$$

where

$$\mathbf{Q} = [\rho \quad \rho u \quad \rho v \quad \rho E]^T \quad (2)$$

$$\mathbf{F} = [\rho u \quad \rho u^2 + P \quad \rho u v \quad \rho u H]^T \quad (3)$$

$$\mathbf{G} = [\rho v \quad \rho u v \quad \rho v^2 + P \quad \rho v H]^T \quad (4)$$

Suitable boundary conditions are applied along the whole or part of the boundary $\Gamma = \Gamma_s + \Gamma_o$ of the domain in Fig. 1. The cost function is a general function of pressure, density, and tangential velocity defined on the body surface as

$$I_c(\mathbf{Q}, X_D) = \int_{\Gamma_s} f(p, \rho, u_s, X_D) ds \quad (5)$$

where u_s and ds are the tangential velocity and the differential arc length, respectively. The augmented cost functional is defined as

$$I = I_c + I_R \quad (6)$$

where

$$I_R = \int_{\Omega} \left(\frac{\partial \mathbf{F}^T}{\partial x} \cdot \lambda + \frac{\partial \mathbf{G}^T}{\partial y} \cdot \lambda \right) d\Omega + \int_{\Gamma_s} \psi(\rho \mathbf{q} \cdot \hat{n}) ds \quad (7)$$

Equation (7) is the volume integral to enforce the conservation equations and the wall boundary condition as constraints of the problem, where \mathbf{q} denotes the fluid velocity. The following lemma for the material derivative¹⁶ is used to find the first-order variation of volume and surface integrals in Eqs. (5) and (7).

Lemma: Let ψ_1, ψ_2, ψ_3 be functionals defined as

$$\begin{aligned} \Psi_1 &= \int_{\Omega} g(\mathbf{x}) d\Omega, & \Psi_2 &= \int_{\Gamma} f(\mathbf{x}) ds \\ \Psi_3 &= \int_C f(\mathbf{q} \cdot \hat{t}) |\mathbf{dx}| \end{aligned} \quad (8)$$

where the volume Ω and its bounding surface Γ deform under the action of a prescribed design velocity field \mathbf{V} . The material derivatives are given, respectively, as

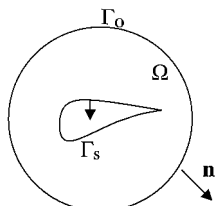


Fig. 1 Domain Ω with design surface Γ_s and outer boundary Γ_o , and their normals.

$$\begin{aligned} \Psi_1 &= \int_{\Omega} \{g'(\mathbf{x}) + \nabla \cdot (g(\mathbf{x}) \mathbf{V}(\mathbf{x}))\} d\Omega \\ &= \int_{\Omega} g'(\mathbf{x}) d\Omega + \int_{\Gamma} g(\mathbf{x}) \mathbf{V} \cdot \hat{n} ds \end{aligned} \quad (9)$$

$$\Psi_2 = \int_C \left(f' + (\mathbf{V} \cdot \hat{n}) \left(\frac{\partial f}{\partial n} - \frac{f}{R} \right) \right) |\mathbf{dx}| + f(\mathbf{V} \cdot \hat{t})|_{x_A}^{x_B} \quad (10)$$

$$\begin{aligned} \Psi_3 &= \int_C \left(f' + (\mathbf{V} \cdot \hat{n}) \left(\frac{\partial f}{\partial n} + \frac{f}{R} \right) + \frac{\partial f}{\partial q_s} \frac{\partial (\mathbf{V} \cdot \hat{n})}{\partial s} q_n \right) |\mathbf{dx}| \\ &\quad + f(\mathbf{V} \cdot \hat{t})|_{x_A}^{x_B} \end{aligned} \quad (11)$$

In Eqs. (9) and (10), f' is the local change in f , and f is the substantial (or total) change in f as the boundary is deformed. Here \hat{t} and \hat{n} are the tangential and normal unit vectors, respectively, \mathbf{x}_A and \mathbf{x}_B are the endpoints of the curve C , and for a closed contour, the last term on the right-hand side of Eqs. (10) and (11) is identically zero.

This lemma is used to obtain the first-order variation of Eq. (6) with respect to the boundary:

$$\begin{aligned} I &= \int_{\Gamma_s} \left(f' + \frac{\partial f}{\partial n} (\mathbf{V} \cdot \hat{n}) + f \frac{(\mathbf{V} \cdot \hat{n})}{R} - f_{u_s} u_n \frac{\partial (\mathbf{V} \cdot \hat{n})}{\partial s} \right) ds \\ &\quad + [f(\mathbf{V} \cdot \hat{t})]_{x_A}^{x_B} - \int_{\Omega} \mathcal{Q}^T (\mathbf{A}^T \cdot \lambda_x + \mathbf{B}^T \cdot \lambda_y) d\Omega \\ &\quad + \int_{\Gamma = \Gamma_s + \Gamma_o} (n_x F' + n_y G') \cdot \lambda ds + \int_{\Gamma_s} \psi \{(\rho \mathbf{q})' \cdot \hat{n} + \rho \mathbf{q} \cdot \hat{n} \\ &\quad + [\mathbf{V} \cdot \nabla(\rho \mathbf{q})] \cdot \hat{n}\} ds \end{aligned} \quad (12)$$

where the partial differentiation operator has been transferred to the Lagrange multipliers by the Gauss theorem. Expanding the last two terms, one can get

$$\begin{aligned} I &= \int_{\Gamma_s} \left(f_p p' + f_{\rho} \rho' + f_{u_s} u_s' + \left(\frac{\partial f}{\partial n} + \frac{f}{R} \right) (\mathbf{V} \cdot \hat{n}) \right) ds \\ &\quad - \int_{\Omega} \mathcal{Q}^T (\mathbf{A}^T \cdot \lambda_x + \mathbf{B}^T \cdot \lambda_y) d\Omega + \int_{\Gamma_o} (n_x F' + n_y G') \cdot \lambda ds \\ &\quad + \int_{\Gamma_s} \Xi(\lambda_1 + u \lambda_2 + v \lambda_3 + H \lambda_4) ds + \int_{\Gamma_s} p'(n_x \lambda_2 + n_y \lambda_3) ds \\ &\quad + \int_{\Gamma_s} \psi \{\Xi + \rho \mathbf{q} \cdot \hat{n} + [\mathbf{V} \cdot \nabla(\rho \mathbf{q})] \cdot \hat{n}\} ds \end{aligned} \quad (13a)$$

where

$$\Xi = n_x (\rho u)' + n_y (\rho v)' \quad (13b)$$

Because for the present problems it is assumed that the flow is steady, inviscid, and adiabatic, the flow is also isentropic along its streamlines, but with different constants before and after the shock. Therefore, density or temperature variations can be easily written in terms of the pressure variation:

$$p' = (\gamma p / \rho) \rho' \quad (14)$$

Furthermore, pressure and tangential velocity are related through the momentum equation in the s direction as follows:

$$\left. \begin{aligned} \frac{\partial p}{\partial s} + \rho u_s \frac{\partial u_s}{\partial s} &= 0 \\ p &= p[s(t, X_D)] \end{aligned} \right\} \Rightarrow p' = -\rho u_s u_s' \quad (15)$$

To extremize the augmented cost functional, its first variation is set to zero. The volume integral in Eq. (13a) is eliminated by

requiring that the Lagrange variables satisfy the following adjoint equation:

$$A^T \cdot \lambda_x + B^T \cdot \lambda_y = 0, \quad \forall \lambda \in \Omega \quad (16)$$

Some of the terms involving the variations of the flow quantities with respect to the boundary can be eliminated by simply setting the following relation to zero:

$$\psi + (\lambda_1 + u\lambda_2 + v\lambda_3 + H\lambda_4) = 0 \quad (17)$$

The surface integrals provide the boundary conditions and the corresponding sensitivity equation (functional derivative). The wall and the far-field boundary conditions are given, respectively, as follows:

$$n_x \lambda_2 + n_y \lambda_3 + f_p + (\rho/\gamma p) f_\rho - f_{u_s} | \rho u_s = 0 \quad (18)$$

$$\int_{\Gamma_O} \mathbf{Q}'^T \cdot \mathbf{A}^T \cdot \lambda = 0 \quad (19)$$

In Eqs. (18) and (19), $\bar{A} = n_x \mathbf{A} + n_y \mathbf{B}$ is the Jacobian matrix associated with the direction of propagation \mathbf{n} . On using the transformations

$$\mathbf{W}' = T^{-1} \cdot \mathbf{Q}' \quad (20)$$

$$\Theta = T^T \cdot \lambda \quad (21)$$

where T is defined by the similarity transformation

$$\bar{A} = T \cdot \bar{\Lambda} \cdot T^{-1} \quad (22)$$

$$\bar{\Lambda} = \text{diag}(v_n, v_n, v_n + c, v_n - c) \quad (23)$$

the far-field boundary condition reduces to

$$\int_{\Gamma_O} \mathbf{W}'^T \cdot \bar{\Lambda} \cdot \Theta \, ds = 0 \quad (24)$$

If the conditions at the far field are kept constant, the characteristic variable W'_i corresponding to the i th eigenvalue will be zero for negative eigenvalues. If Θ_i corresponding to the i th positive eigenvalue of \bar{A} is denoted by Θ_i^+ , the far-field boundary condition will be satisfied if $\Theta_i^+ = 0$. A logic is built in to check the local Mach number and the flow direction with respect to the domain as summarized in Table 1.

Hence, the first-variation of the augmented functional can be computed from the following equation:

$$\begin{aligned} I = & - \int_{\Gamma_S} \Pi \{ \rho \mathbf{q} \cdot \hat{n} + [\mathbf{V} \cdot \nabla(\rho \mathbf{q})] \cdot \hat{n} \} \, ds \\ & + \int_{\Gamma_S} \left(\frac{\partial f}{\partial n} + \frac{f}{R} \right) (\mathbf{V} \cdot \hat{n}) \, ds \end{aligned} \quad (25)$$

where

$$\Pi = \lambda_1 + u\lambda_2 + v\lambda_3 + H\lambda_4 \quad (26)$$

In Eq. (25), the gradient of $\rho \mathbf{q}$ on the control surface needs to be computed accurately. The cell-centered control volume on linear triangles represents the curved airfoil surface with piecewise linear segments. The well-known Babuska paradox (see Ref. 17) states that when linear segments are used to approximate a curved boundary the directional derivatives with components along the normal direction

Table 1 Physical and numerical boundary conditions at the far field

Outlet/inlet	Physical conditions	Numerical conditions
Subsonic outlet	$\theta_1, \theta_2, \theta_3$	θ_4
Supersonic outlet	$\theta_1, \theta_2, \theta_3, \theta_4$	None
Subsonic inlet	θ_3	$\theta_1, \theta_2, \theta_4$
Supersonic inlet	None	$\theta_1, \theta_2, \theta_3, \theta_4$

will almost always converge to the wrong answer. In the following, it will be shown that a switch to body-fitted coordinates $s-n$, in conjunction with the reduction of the governing state equation to the control surface, results in sensitivity integrals that are only a function of the tangential derivatives of the state variables. These tangential derivatives can be computed very accurately with cubic spline fitting of the available information on the surface, and furthermore, this approach eliminates the need for normal derivative computations that can be erroneous.

However, certain control surface parameterizations result in unidirectional design velocity fields and any proposed formulation must be able to take the utmost advantage of this simplifying condition. As such, two slightly different approaches can be used: 1) full transformation to the $s-n$ plane and 2) coexistence of the Cartesian and $s-n$ coordinate systems in the formulation. In the first approach, one can show by straightforward algebraic manipulations that for a two-dimensional curve in the $s-n$ coordinates

$$\hat{n} = \left(\frac{\partial(V \cdot \hat{n})}{\partial s} - \frac{V \cdot \hat{t}}{R} \right) \hat{t} = \theta' \hat{t} \quad (27)$$

where θ is the angle between the tangent and the positive x axis. Also, the convective derivative term of Eq. (25) can be written as

$$[\mathbf{V} \cdot \nabla(\rho \mathbf{q})] \cdot \hat{n} = \left(-\frac{\partial}{\partial s} (\rho u_n) + \frac{\rho u_s}{R} \right) (\mathbf{V} \cdot \hat{t}) - \frac{\partial}{\partial n} (\rho u_n) (\mathbf{V} \cdot \hat{n}) \quad (28)$$

The normal derivative term in Eq. (28) can be eliminated by using the continuity equation in the $s-n$ coordinate system:

$$\frac{\partial}{\partial s} (\rho u_s) + \frac{\partial}{\partial n} (\rho u_n) - \frac{\rho u_n}{R} = 0 \quad (29)$$

Furthermore, for a solid wall with no suction or blowing, Eq. (28) can be further simplified as

$$[\mathbf{V} \cdot \nabla(\rho \mathbf{q})] \cdot \hat{n} = \mathbf{V} \cdot \left(\frac{\rho u_s}{R} \hat{t} + \frac{\partial}{\partial s} (\rho u_s) \hat{n} \right) \quad (30)$$

Substituting Eqs. (27) and (29) back into Eq. (25) yields

$$\begin{aligned} I = & - \int_{\Gamma_S} \Pi \left(\rho u_s \theta' + \frac{\rho u_s}{R} (\mathbf{V} \cdot \hat{t}) + \frac{\partial}{\partial s} (\rho u_s) (\mathbf{V} \cdot \hat{n}) \right) \, ds \\ & + \int_{\Gamma_S} \left(\frac{\partial f}{\partial n} + \frac{f}{R} \right) (\mathbf{V} \cdot \hat{n}) \, ds \end{aligned} \quad (31)$$

In the second approach, the convective derivative term of Eq. (25) takes the following form in Cartesian coordinates:

$$[\mathbf{V} \cdot \nabla(\rho \mathbf{q})] \cdot \hat{n} = \mathbf{V} \cdot [n_x \nabla(\rho u) + n_y \nabla(\rho v)] \quad (32)$$

The Cartesian components of Eq. (32) can be found very easily by applying a rotation of axis to the results of Eq. (30):

$$n_x \nabla(\rho u) + n_y \nabla(\rho v) = \begin{bmatrix} \kappa \rho u_s \cos \theta - \sin \theta \frac{\partial(\rho u_s)}{\partial s} \\ \kappa \rho u_s \sin \theta + \cos \theta \frac{\partial(\rho u_s)}{\partial s} \end{bmatrix} \quad (33)$$

Therefore, the final form of the sensitivities for the second approach is

$$\begin{aligned} I = & - \int_{\Gamma_S} \Pi \left\{ \rho u_s \theta' + \left(\kappa \rho u_s \cos \theta - \sin \theta \frac{\partial(\rho u_s)}{\partial s} \right) (\mathbf{V} \cdot \hat{t}) \right. \\ & \left. + \left(\kappa \rho u_s \sin \theta + \cos \theta \frac{\partial(\rho u_s)}{\partial s} \right) (\mathbf{V} \cdot \hat{j}) \right\} \, ds \\ & + \int_{\Gamma_S} \left(\frac{\partial f}{\partial n} + \frac{f}{R} \right) (\mathbf{V} \cdot \hat{n}) \, ds \end{aligned} \quad (34)$$

As is apparent from Eqs. (31) and (34), the normal derivatives of flow quantities to the control surface only appear implicitly in the normal derivative of the cost functional. Accurate computation of these derivatives is discussed subsequently.

The method of approach here is first to write the Euler equations (1) in s - n coordinates and then to recast them in a way that relates normal derivatives of flow variables to expressions involving only the tangential derivatives. Therefore, the governing equations (1) in the s - n coordinates are

$$\frac{\partial}{\partial s}(\rho u_s) + \frac{\partial}{\partial n}(\rho u_n) - \frac{\rho u_n}{R} = 0 \quad (35)$$

$$\frac{\partial p}{\partial s} + \rho u_s \frac{\partial u_s}{\partial s} + \rho u_n \left(1 + \frac{n}{R}\right) \frac{\partial u_s}{\partial n} + \frac{\rho u_s u_n}{R+n} = 0 \quad (36)$$

$$\frac{\partial p}{\partial n} - \frac{\rho u_s^2}{R+n} + \frac{\rho u_s}{1+n/R} \frac{\partial u_n}{\partial s} + \rho u_n \frac{\partial u_n}{\partial n} = 0 \quad (37)$$

$$\frac{\partial}{\partial s}(\rho u_s H) + \frac{\partial}{\partial n} \left(\frac{R \rho u_n H}{n+R} \right) = 0 \quad (38)$$

Also, note that on the surface, where $n = 0$, the normal component of velocity u_n vanishes. The normal derivative of pressure can be found directly from the normal momentum equation as

$$\frac{\partial p}{\partial n} = \frac{\rho u_s^2}{R} \quad (39)$$

Normal derivatives of density and tangential velocity are more involved. The energy equation on the airfoil surface can be simplified to show that the total enthalpy is constant throughout the flowfield before and after the shock:

$$H = C_p T + u_s^2/2 = \text{const} \quad (40)$$

Equation (40) cannot be differentiated with respect to n because it is valid only at $n = 0$. However, if $u_s^2/2$ is replaced by $(u_s^2 + u_n^2)/2$ in Eq. (40), then it can be differentiated with respect to n , and, thereby, to provide the following relationship between the normal derivatives of density, pressure, and tangential velocity on the airfoil surface:

$$\frac{\partial \rho}{\partial n} = \frac{\gamma}{a^2} \frac{\partial p}{\partial n} + \frac{\rho u_s}{a^2} (\gamma - 1) \frac{\partial u_s}{\partial n} \quad (41)$$

If the tangential momentum equation is differentiated with respect to n and the normal derivatives of pressure and density are substituted from Eqs. (39) and (41), respectively, the following first-order differential equation is obtained:

$$\begin{aligned} \frac{\partial}{\partial s} \left(\frac{\partial u_s}{\partial n} \right) + \left(\frac{\partial u_s}{\partial n} \right) \left(\frac{u_s}{a^2} (\gamma - 1) \frac{\partial u_s}{\partial s} - \frac{1}{\rho} \frac{\partial \rho}{\partial s} \right) \\ = - \frac{\partial}{\partial s} \left(\frac{u_s}{R} \right) - \frac{\gamma}{a^2} \frac{u_s^2}{R} \frac{\partial u_s}{\partial s} \end{aligned} \quad (42)$$

The source term and the coefficient of the normal derivative of u_s are known functions of s from the CFD analysis. Hence, this equation can be solved for the normal derivative of u_s with a periodic boundary condition. Consequently, the normal derivative of density can be found by substituting for the normal derivatives of pressure and tangential velocity in Eq. (41).

Sensitivities with Surface Parameterization

A nonparametric geometry definition requires the surface mesh coordinates. Although this approach utilizes the readily available data, it increases the number of design variables. However, a parametric geometry definition reduces the number of design variables because the number of control points is significantly less than the surface mesh points. They do require some understanding in making the choice of parameterization technique, as well as extra computations and storage. In the present approach, an m th-degree Bezier-

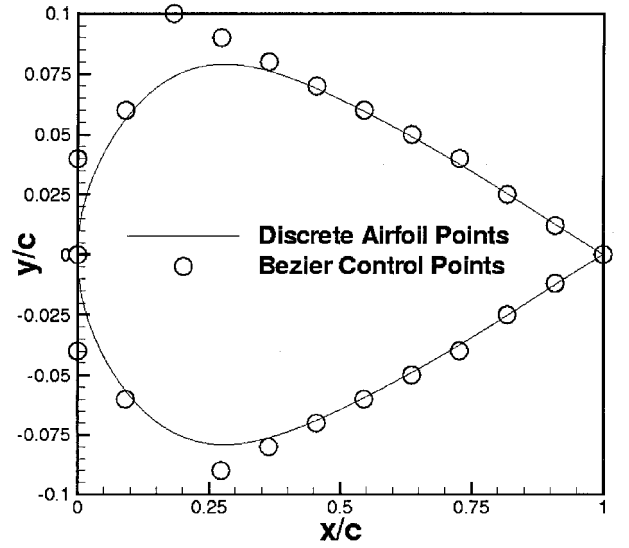


Fig. 2a Bezier control points for the initial airfoil.

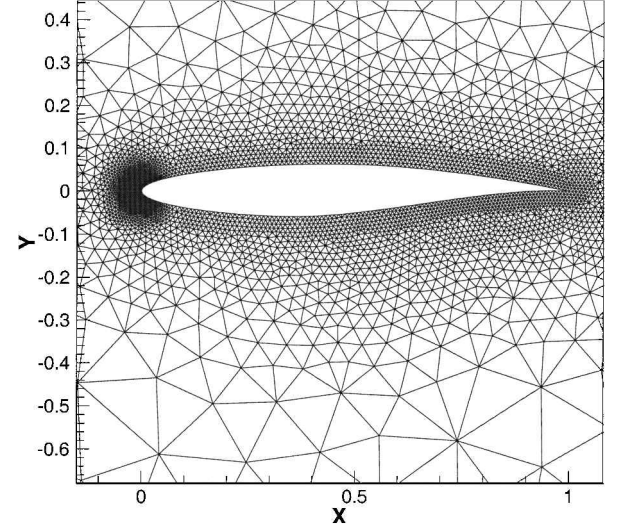


Fig. 2b Unstructured mesh for the target airfoil design.

Bernstein representation (Fig. 2a) is obtained using a parameter t as follows:

$$\mathbf{R}(t) = \sum_{i=0}^m B_i^m(t) \mathbf{P}_i, \quad t \in [0, 1] \quad (43)$$

where

$$\mathbf{P}_i = (X_i \quad Y_i), \quad \mathbf{R}(t) = (x \quad y) \quad (44)$$

$$B_i^m(t) = \binom{m}{i} t^i (1-t)^{m-i} = \frac{m!}{i!(m-i)!} t^i (1-t)^{m-i} \quad (45)$$

The variation of a point on a design surface requires the perturbations of the control points, which are related to the surface mesh coordinates by

$$\mathbf{V} = \sum_{i=0}^m B_i^m(t) \mathbf{P}'_i = \sum_{i=0}^m B_i^m(t) \begin{pmatrix} X'_i \\ Y'_i \end{pmatrix} \quad (46)$$

If the unit normal is given by

$$\hat{\mathbf{n}} = \begin{pmatrix} \dot{y} & -\dot{x} \\ \sqrt{\dot{x}^2 + \dot{y}^2} & \sqrt{\dot{x}^2 + \dot{y}^2} \end{pmatrix}^T \quad (47)$$

then the design derivative of the unit normal can be written as

$$\dot{\hat{\mathbf{n}}} = \theta' \hat{\mathbf{t}} = \frac{\dot{y}' \dot{x} - \dot{x}' \dot{y}}{\dot{x}^2 + \dot{y}^2} \hat{\mathbf{t}} \quad (48)$$

Finally, the sensitivity equation, that is, the variation of the cost functional with respect to the ordinates of the Bezier control points, is obtained by incorporating Eqs. (43–48) into Eq. (34):

$$\begin{aligned} \frac{\partial I}{\partial Y_i} = & - \int_0^1 \Pi Q_2 \frac{dB_i^m}{dt} dt \\ & - \int_0^1 \Pi \frac{B_i^m}{\sqrt{\dot{x}^2 + \dot{y}^2}} \left(\dot{x}\ddot{y} - \dot{y}\ddot{x} \right) \dot{y} (Q_2 \dot{x} + Q_3 \dot{y}) + \dot{x} \frac{\partial(\rho u_s)}{\partial s} dt \\ & + \int_0^1 \left(\frac{\partial f}{\partial n} B_i^m \sqrt{\dot{x}^2 + \dot{y}^2} - f \frac{\dot{x}\ddot{y} - \dot{y}\ddot{x}}{\dot{x}^2 + \dot{y}^2} B_i^m \right) ds \quad (49) \end{aligned}$$

Solving State and Costate Equations

The state equation (1) is first expressed in the integral form for a bounded domain Ω with a boundary Γ (Fig. 1):

$$\frac{\partial}{\partial t} \int_{\Omega} \mathbf{Q} d\Omega + \int_{\Gamma} (n_x A_i^T + n_y B_i^T) \cdot \mathbf{Q} d\Gamma = 0 \quad (50)$$

Second-order spatial discretization for the present upwind scheme is accomplished by using Roe's flux-difference splitting. Cell-centered solutions are Taylor-series expanded to each of the faces of each triangular cell in the domain (Fig. 2b). The spatially discretized form of the governing equations are then integrated in pseudotime using the explicit four-stage Runge–Kutta method. On the wall, the standard inviscid boundary conditions Γ_s for the velocity and the pressure are implemented: impermeable, velocity parallel to the wall, and zero pressure gradient. In the farfield, characteristic boundary conditions Γ_o are employed based on the locally one-dimensional Riemann invariants.

For the adaptation of the mesh to the boundary changes as the shape evolves, the tension-springs analogy is used, that is, each edge of a triangle is represented by a tension spring. By assuming that the spring stiffness is inversely proportional to the edge length, the equilibrium of the composite spring forces provides the displacement of each node. To restrict the size of the adaptation region, a window is created around a boundary being reshaped. The entire domain is searched to locate the window nodes and the window frame nodes. Then, the window nodes are allowed to be adapted, but the nodes exterior to the window and the window frame nodes are spatially fixed. Detailed discussions of the solution algorithm may be found in Refs. 18 and 19.

The adjoint equations (16) are of the same order and character as the flow (state) equations (1). Hence, they are discretized and solved for the Lagrange variable vector λ by the same CFD scheme used for the flow equations. However, to facilitate this pseudotime marching scheme, a pseudotime term is added:

$$\frac{\partial \lambda}{\partial t} - A^T \lambda_x - B^T \lambda_y = 0 \quad (51)$$

then expressed in the integral form for a bounded domain Ω and its boundary Γ (Fig. 1):

$$\frac{\Delta \Omega_i}{\Delta t} (\lambda_i^{n+1} - \lambda_i^n) - \int_{\Gamma} (n_x A_i^T + n_y B_i^T) \cdot \lambda ds = 0 \quad (52)$$

The Jacobians in Eq. (52) are calculated at the cell centers and they are taken outside the integral sign. If the Jacobian matrix associated with direction \mathbf{n} is denoted by

$$n_x A_i^T + n_y B_i^T = \bar{A}(\mathbf{Q}_i; \hat{n}) \quad (53)$$

then the spatial term in Eq. (52) can be rewritten as

$$\int_{\Gamma} (n_x A_i^T + n_y B_i^T) \cdot \lambda ds = \sum_{j \in N_i} G_{ij} l_{ij} \quad (54)$$

In Eq. (54), l_{ij} is the side of cell i lying between the cell i and the neighboring cell j , and G_{ij} for a cell-centered scheme can be written as

$$G_{ij} = \frac{1}{2} [\bar{A}(\mathbf{Q}_i; \hat{n})(\lambda_l + \lambda_r) + |\bar{A}|^T(\lambda_r - \lambda_l)] \quad (55)$$

where $|\bar{A}|$ is the Jacobian matrix evaluated at the Roe state and the left and right values are the cell quantities extended to the sides by the Taylor series expansion around the cell center.

Optimization

The gradient-based and constrained optimization method of Kreisselmeier–Steinhauser (KS)²⁰ as coded in KSOPT²¹ is used. This method converts all of the equality constraints into a set of inequality constraints; then it combines the objective function and all of the inequality constraints into one composite KS function. That is, the constrained problem is converted to an unconstrained one using the KS function rather than the traditional penalty method. The gradient of the composite KS function is then generated using the analytical sensitivities from Eq. (49). At this point a sequential unconstrained minimization technique is used. The particular choice herein is the Davidson–Fletcher–Powell search algorithm for the univariate search direction and the optimum step size. The stopping criterion is selected to be the relative change of the composite KS function to be less than a prescribed amount in three consecutive iterations. Although not used herein, this method can handle multiple objective functions.

Demonstration of Methodology

The analytically computed sensitivities are compared with the benchmark of finite difference derivatives. Because the discretization error of the continuous formulation does not correspond to that of the state equations, only in the limit when the mesh size approaches zero, the continuous sensitivities are expected to approach asymptotically the finite difference derivatives. In Fig. 3, it is demonstrated that the continuous adjoint sensitivities compare well with the finite difference derivatives for the fairly fine mesh employed herein.

This new continuous adjoint formulation, which is coupled with a CFD solver, optimizer, surface parameterizer, and mesh movement module, will now be demonstrated. Three cases are considered, where the shape of an airfoil is optimized for different objective functions f as assigned to the cost function [Eq. (5)]. In all three cases, the Bezier control points \mathbf{p}_i of Eq. (44) are treated as the design variables, and side constraints are assigned to the y coordinate of each one of the knots Y_i of Eq. (49). Also, geometric constraints can be applied to control, for example, the trailing edge included angle, maximum thickness, thickness at midchord, or included area.

Each optimization cycle starts with a symmetric NACA 0012 profile (Fig. 2a) as the initial design. A steady-state solution is obtained for the airfoil at 2-deg angle of attack in Mach 0.75 flow. For the sake of driving the optimization, the target aerodynamics is obtained from the solution of the flow at the same conditions but for an Royal Aircraft Establishment profile. This target profile and its

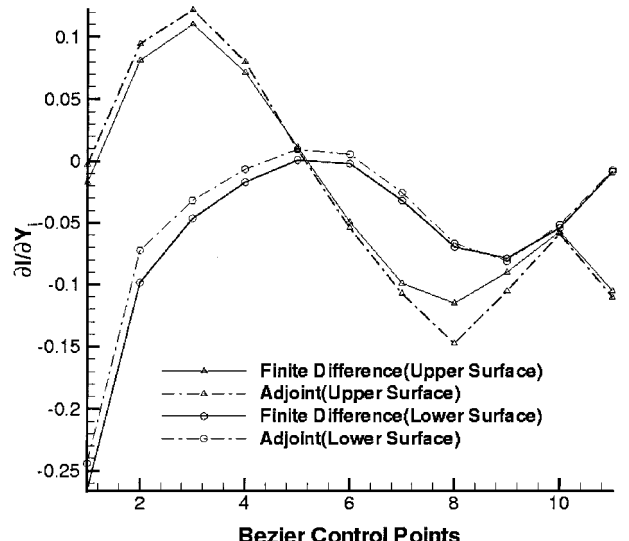


Fig. 3 Computed continuous adjoint sensitivities vs benchmark finite difference (brute force) derivatives.

unstructured mesh is shown in Fig. 2b. The mesh has 14,590 cells (7480 nodes) and there are 370 nodes on the airfoil, which is the design surface. The airfoil is Bezier-Bernstein parameterized with 24 Bezier control points, of which 22 are used as the design variables (Fig. 2a).

Case 1 is the minimization of the departure from the target pressure distribution as denoted by p' :

$$f = \frac{1}{2}(p - p')^2 \quad (56)$$

This is a typical case performed by others, for example, in Ref. 10. Presented in Figs. 4a-4c are the surface pressure distributions, shape evolution, and the variation of the cost functional for case 1. Each Figures 4a-4c include respective plots for the initial and target profiles and those that correspond to two intermediate and the final designs. The maximum deviation between the target and the final profile is less than 1.75%, which is very satisfactory. Point by point recovery of the target profile is not expected because continuous adjoint sensitivities agree with brute-force derivatives only in the limit of an infinitely fine mesh (Fig. 3). Although the results are very close to the target after 30 flow analyses and 5 gradient evaluations, with the shock locations coincident, the residual of the cost functional does not meet the stopping criterion. It is only after another 45 analyses and 5 gradient evaluations that the optimization process terminates.

Case 2 is selected to demonstrate that the present formulation is general and that the cost functional does not have to include pressure. In Ref. 22, it is noted that such a generalized cost functional is necessary and possible. The objective now is the minimization of the departure from the target density distribution as denoted by ρ' :

$$f = \frac{1}{2}(\rho - \rho')^2 \quad (57)$$

Presented in Figs. 5a-5c are the surface density distributions, shape evolution, and the variation of the cost functional for case 2. Figures 5a-5c include respective plot for the initial and target profiles and those that correspond to one intermediate and the final designs. The final design and its pressure distribution are again virtually identical to the target. However, the slow convergence to the solution when the search is near the solution, as observed in case 1, repeats itself.

Finally, case 3 is considered to demonstrate a composite cost functional that includes an aerodynamic constraint through a penalty coefficient. The drag is added to the cost functional of case 1 after multiplying it by the coefficient Λ , which is assigned an arbitrary value of 0.1:

$$f = \frac{1}{2}(p - p')^2 ds + \Lambda C_d \quad (58)$$

Presented in Figs. 6a-6c are the surface pressure distributions, shape evolution, and the history of the lift and drag for case 3. Figures 6a-6c include respective plot for the initial and target profiles and those that correspond to three intermediate and the final designs. Because this case is not only a minimization of a departure from the target but also a drag minimization, the final shape is not known a priori, that is, blind optimization. Instead, the profile that supports the target pressure distribution [the first term in Eq. (58)] is overlaid on Figs. 6a-6c. The final design has the upper surface shock at about the same location as the target shape because the optimization process is trying to match the prescribed target pressure distribution, and at the same time it is also trying to reduce the shock strength, which is responsible for the inviscid pressure drag. For the optimized profile, the ratio of the pressure coefficient downstream of the shock to the corresponding value upstream of the shock is approximately equal to 1.45, whereas the same ratio for the prescribed pressure profile is about 2.15. This explains the reduction in inviscid drag coefficient from 0.0170 for the prescribed pressure distribution to about 0.0095 for the optimized profile.

All of these demonstrations are produced on a small desktop computer. This is possible because generating the continuous sensitivities requires no additional memory beyond that for the flow analysis (for the present cases, it is 65 MB). Unlike solving for the discrete sensitivities,^{23,24} here there is no need to form any large matrices. To avoid such large matrices, an approximate factorization was used for the discrete adjoint equations in Ref. 5, but at some

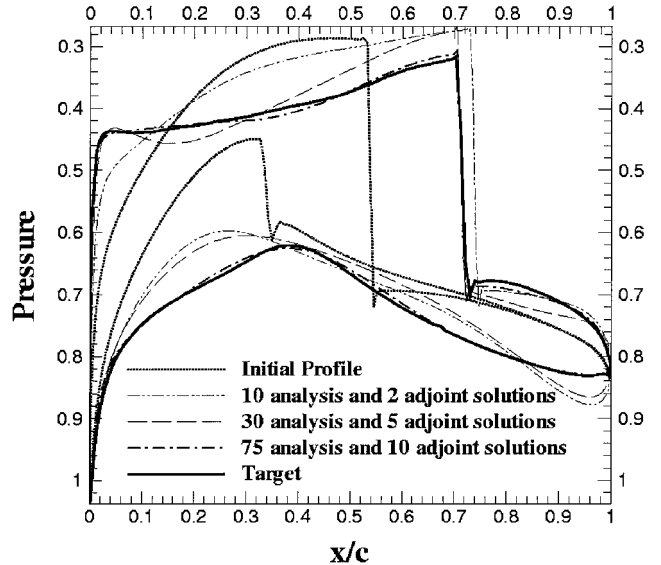


Fig. 4a History of surface pressure distributions for case 1: minimization of surface pressure departure from the target profile.

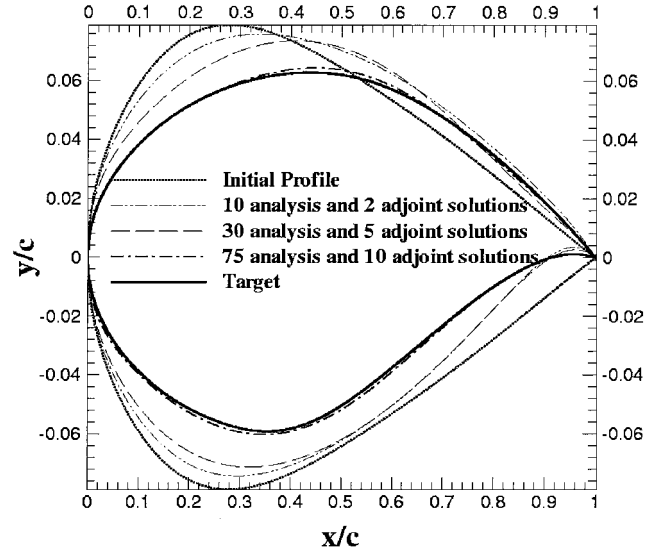


Fig. 4b Evolution of airfoil shapes during optimization for case 1: minimization of surface pressure departure from the target profile.

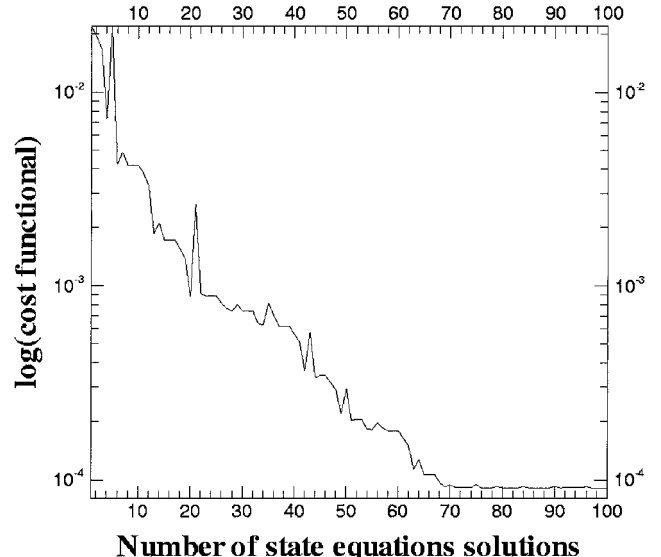


Fig. 4c Convergence history during the optimization for case 1: minimization of surface pressure departure from the target profile.

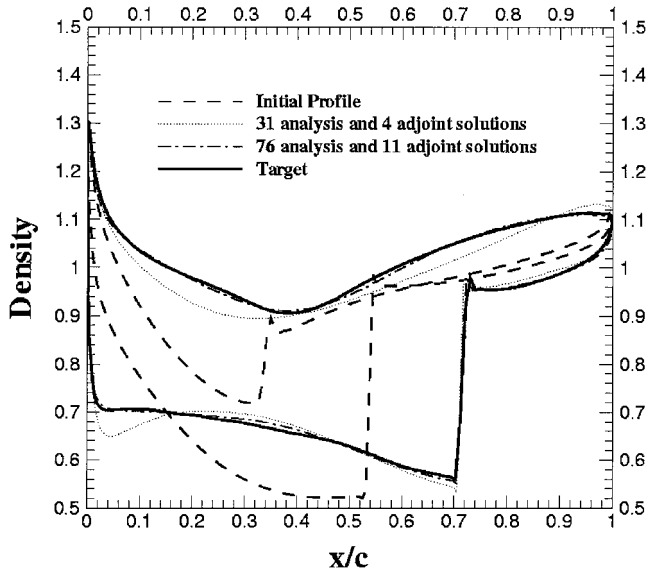


Fig. 5a History of surface density distributions for case 2: minimization of surface density departure from the target profile.

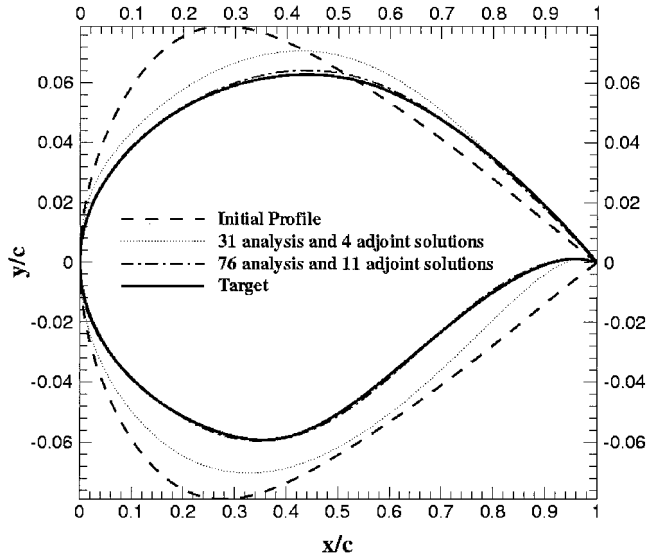


Fig. 5b Evolution of airfoil shapes during optimization for case 2: minimization of surface density departure from the target profile.

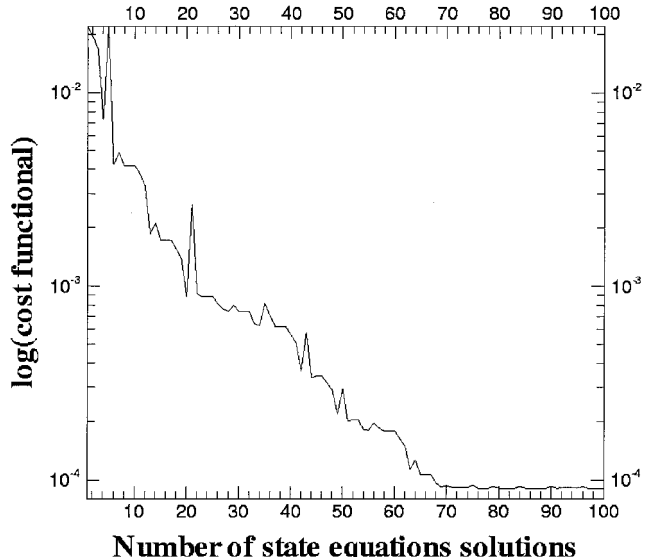


Fig. 5c Convergence history during the optimization for case 2: minimization of surface density departure from the target profile.

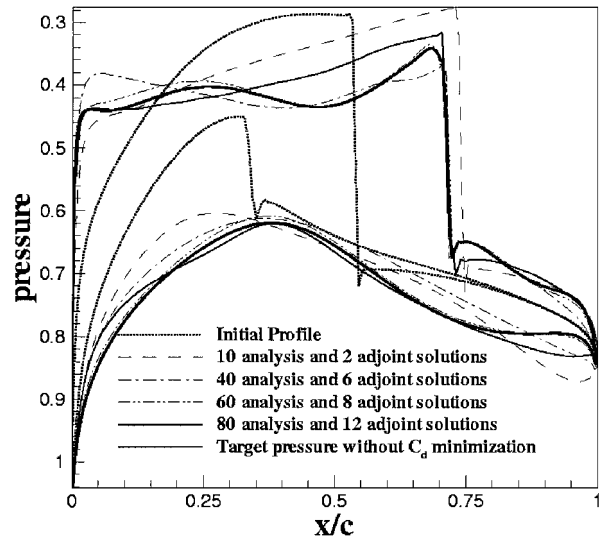


Fig. 6a History of surface pressure distributions for case 3: minimization of drag and surface pressure departure from the target profile.

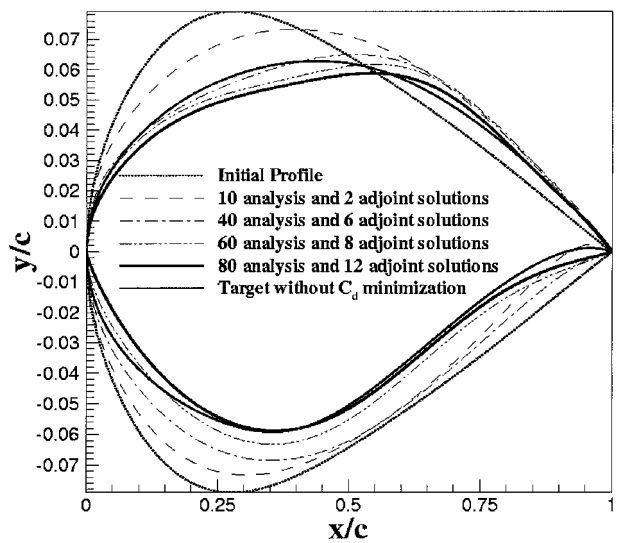


Fig. 6b Evolution of airfoil shapes during optimization for case 3: minimization of drag and surface pressure departure from the target profile.

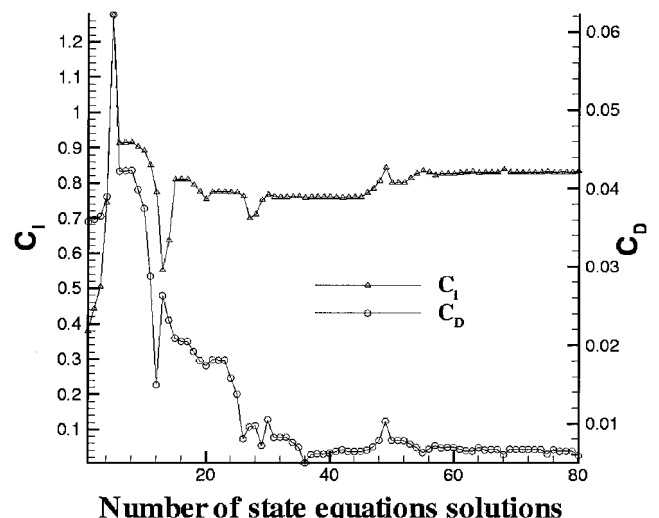


Fig. 6c History of lift and drag for case 3: minimization of drag and surface pressure departure from the target profile.

expense of the convergence rates. In the present continuous adjoint method, the average computational time needed for one design cycle is about 1.8 times that for one flow analysis. A final comparison point is the amount of work needed to produce the code that generates the sensitivities. Once the formulation is well understood, the present hand differentiation is roughly the same amount of labor as it is for hand differentiation to obtain the discrete sensitivities. Automatic differentiation for the discrete sensitivities (e.g., Ref. 13) would be less laborious. However, current automatic differentiation algorithms produce some unnecessary terms along with those that generate the gradients, which leads to further degradation of the computing times.

Conclusions

An adjoint approach is developed to obtain the continuous sensitivity derivatives of the Euler equations and general cost functionals. Both the state and the costate equations are second-order finite volume discretized for unstructured meshes, and they are coupled with a constrained optimization algorithm. Also integrated into the overall methodology are a geometry parameterization method for the shape optimization and a dynamic unstructured mesh method for the shape evolution and the consequent volume mesh adaptations. For the proof of concept, three airfoil optimization problems in transonic flow are presented. These results should establish 1) the generality of the method in accepting cost functions, 2) the accuracy of the obtained sensitivity derivatives, and 3) the efficiency with which the optimized shapes are obtained on a small desktop computer. Consequently, the method is suitable and is being extended for the unsteady flows and aeroacoustics.

References

- ¹Baysal, O. (ed.), *Multidisciplinary Applications of Computational Fluid Dynamics*, Fluid Engineering Div., Vol. 129, American Society of Mechanical Engineers, Fairfield, NJ, 1991.
- ²Baysal, O. (ed.), *CFD for Design and Optimization*, Fluid Engineering Div., Vol. 232, American Society of Mechanical Engineers, Fairfield, NJ, 1995.
- ³Johnson, G., Baysal, O., and Lee, Y.-T. (ed.), "Design Optimization Using CFD," *Proceedings of Fluids Engineering Division Summer Meeting [CD-ROM]*, Fluid Engineering Div., American Society of Mechanical Engineers, Fairfield, NJ, 1997.
- ⁴Eleshaky, M. E., and Baysal, O., "Shape Optimizing Nacelle Near Flat-Plate Wing Using Multiblock Sensitivity Analysis," *Journal of Aircraft*, Vol. 35, No. 1, 1998, pp. 33-38.
- ⁵Pandya, M. J., and Baysal, O., "Three-Dimensional Viscous ADI Algorithm and Strategies for Shape Optimization," *Proceedings of AIAA 13th CFD Conference*, AIAA, Reston, VA, 1997, pp. 475-485.
- ⁶Huan, J., and Modi, V., "Design of Minimum Drag Bodies in Incompressible Laminar Flow," *CFD for Design and Optimization*, edited by O. Baysal, Fluid Engineering Div., Vol. 232, American Society of Mechanical Engineers, Fairfield, NJ, 1995, pp. 37-44.
- ⁷Reuther, J., and Jameson, A., "Supersonic Wing and Wing-Body Shape Optimization Using an Adjoint Formulation," *CFD for Design and Optimization*, edited by O. Baysal, Fluid Engineering Div., Vol. 232, American Society of Mechanical Engineers, Fairfield, NJ, 1995, pp. 45-52.
- ⁸Elliott, J., and Peraire, J., "Practical 3D Aerodynamic Design and Optimization Using Unstructured Meshes," AIAA Paper 96-4170, 1996.
- ⁹Matsuzawa, T., and Hafez, M., "Treatment of Shock Waves in Design Optimization via Adjoint Equation Approach," AIAA Paper 98-2537, 1998.
- ¹⁰Anderson, W. K., and Venkatakrishnan, V., "Aerodynamic Design Optimization on Unstructured Grids with a Continuous Adjoint Formulation," AIAA Paper 97-0643, Jan. 1997.
- ¹¹Baysal, O., and Eleshaky, M. E., "Aerodynamic Design Optimization Using Sensitivity Analysis and Computational Fluid Dynamics," *AIAA Journal*, Vol. 30, No. 3, 1992, pp. 718-725.
- ¹²Baysal, O., "Methods for Sensitivity Analysis in Gradient-Based Shape Optimization—A Review," *Proceedings of Fluids Engineering Division Summer Meeting [CD-ROM]*, Fluid Engineering Div., American Society of Mechanical Engineers, Fairfield, NJ.
- ¹³Baysal, O., Cordero, Y., and Pandya, M. J., "Improving Discrete-Sensitivity-Based Approach for Practical Design Optimization," *Proceedings of JSME Fluid Engineering Conference*, Vol. 1, Japanese Society of Mechanical Engineers, Tokyo, 1997, pp. 417-424.
- ¹⁴Ibrahim, A. H., and Baysal, O., "Design Optimization Using Variational Methods and CFD," AIAA Paper 94-0093, Jan. 1994.
- ¹⁵Ghayour, K., "Aerodynamic Optimisation Using Design Sensitivity Analysis," M.Sc. Thesis, Dept. of Aeronautical Engineering, Imperial College of Science, Technology and Medicine, London.
- ¹⁶Haug, E. J., Choi, K. K., and Komkov, V., *Design Sensitivity Analysis of Structural Systems*, Academic Press, Orlando, FL, 1986, pp. 190-201.
- ¹⁷Strang, G., and Fix, G. J., *An Analysis for the Finite Element Method*, Prentice-Hall, Englewood Cliffs, NJ, 1973, pp. 60-64.
- ¹⁸Singh, K. P., Newman, J. C., III, and Baysal, O., "Dynamic Unstructured Method for Flows Past Multiple Objects in Relative Motion," *AIAA Journal*, Vol. 33, No. 4, 1995, pp. 641-659.
- ¹⁹Baysal, O., and Luo, X.-B., "Dynamic Unstructured Method for Relative Motion of Multibody Configuration at Hypersonic Speeds," *Journal of Aircraft*, Vol. 36, No. 4, 1999, pp. 725-729.
- ²⁰Kreisselmeier, G., and Steinhauser, R., "Systematic Control Design by Optimizing a Vector Performance Index," *Proceedings of IFAC Symposium on Computer Aided Design of Control Systems*, 1979, pp. 113-117.
- ²¹Wrenn, G. A., "An Indirect Method for Numerical Optimization Using the Kreisselmeier-Steinhaus Function," NASA CR-4220, March 1989.
- ²²Arian, E., and Salas, M., "Admitting the Inadmissible: Adjoint Formulation for Incomplete Cost Functionals in Aerodynamic Optimization," Inst. for Computer Applications in Science and Engineering, ICASE Rept. 97-69, NASA CR-206269, Hampton, VA, 1997.
- ²³Burgreen, G. W., and Baysal, O., "Three-Dimensional Aerodynamic Shape Optimization Using Discrete Sensitivity Analysis," *AIAA Journal*, Vol. 34, No. 9, 1996, pp. 1761-1770.
- ²⁴Item, C. C., and Baysal, O., "Wing-Section Optimization for Supersonic Viscous Flow," *Journal of Fluids Engineering*, Vol. 120, No. 1, 1998, pp. 102-108.

A. Chattopadhyay
Associate Editor